spectroscopy journal

MDPI

Article

Infrared Spectroscopy and Photochemistry of Ethyl Maltol in Low-Temperature Argon Matrix

İsa Sıdır [1,2,*], Susy Lopes [2], Timur Nikitin [2], Yadigar Gülseven Sıdır [1,2] and Rui Fausto [2,3,*]

[1] Department of Physics, Bitlis Eren University, 13000 Bitlis, Türkiye; ygsidir@beu.edu.tr
[2] CQC-IMS, Department of Chemistry, University of Coimbra, 3004-535 Coimbra, Portugal; susylopes@qui.uc.pt (S.L.)
[3] Department of Physics, Faculty Sciences and Letters, Istanbul Kultur University, 34158 Bakirkoy, Istanbul, Türkiye
* Correspondence: author isidir@beu.edu.tr (İ.S.); rfausto@ci.uc.pt (R.F.)

Abstract: Ethyl maltol was investigated using matrix isolation infrared spectroscopy and DFT calculations. In an argon matrix (14.5 K), the compound was found to exist in a single conformer (form I), characterized by an intramolecular hydrogen bond with an estimated energy of ~17 kJ mol^{-1}. The IR spectrum of this conformer was assigned, and the molecule's potential energy landscape was explored to understand the relative stability and isomerization dynamics of the conformers. Upon annealing the matrix to 41.5 K, ethyl maltol was found to predominantly aggregate into a centrosymmetric dimer (2× conformer I) bearing two intermolecular hydrogen bonds with an estimated energy of ca. 28 kJ mol^{-1} (per bond). The UV-induced ($\lambda > 235$ nm) photochemistry of the matrix-isolated ethyl maltol was also investigated. After 1 min of irradiation, band markers of two rearrangement photoproducts formed through the photoinduced detachment-attachment (PIDA) mechanism, in which the ethyl maltol radical acts as an intermediate, were observed: 1-ethyl-3-hydroxy-6-oxibicyclo [3.1.0] hex-3-en-2-one and 2-ethyl-2*H*-pyran-3,4-dione. The first undergoes subsequent reactions, rearranging to 4-hydroxy-4-propanoylcyclobut-2-en-1-one and photofragmenting to cyclopropenone and 2-hydroxybut-1-en-1-one. Other final products were also observed, specifically acetylene and CO (the expected fragmentation products of cyclopropenone), and CO_2. Overall, the study demonstrated ethyl maltol's high reactivity under UV irradiation, with significant photochemical conversion occurring within minutes. The rapid photochemical conversion, with complete consumption of the compound in 20 min, should be taken into account in designing practical applications of ethyl maltol.

Keywords: ethyl maltol; matrix isolation; infrared spectra; H-bonding; photochemistry

check for updates

Citation: Sıdır, İ.; Lopes, S.; Nikitin, T.; Gülseven Sıdır, Y.; Fausto, R. Infrared Spectroscopy and Photochemistry of Ethyl Maltol in Low-Temperature Argon Matrix. *Spectrosc. J.* **2024**, *2*, 188–205. https://doi.org/10.3390/spectroscj2040013

Academic Editor: Clemens Burda

Received: 29 August 2024
Revised: 11 September 2024
Accepted: 1 October 2024
Published: 3 October 2024

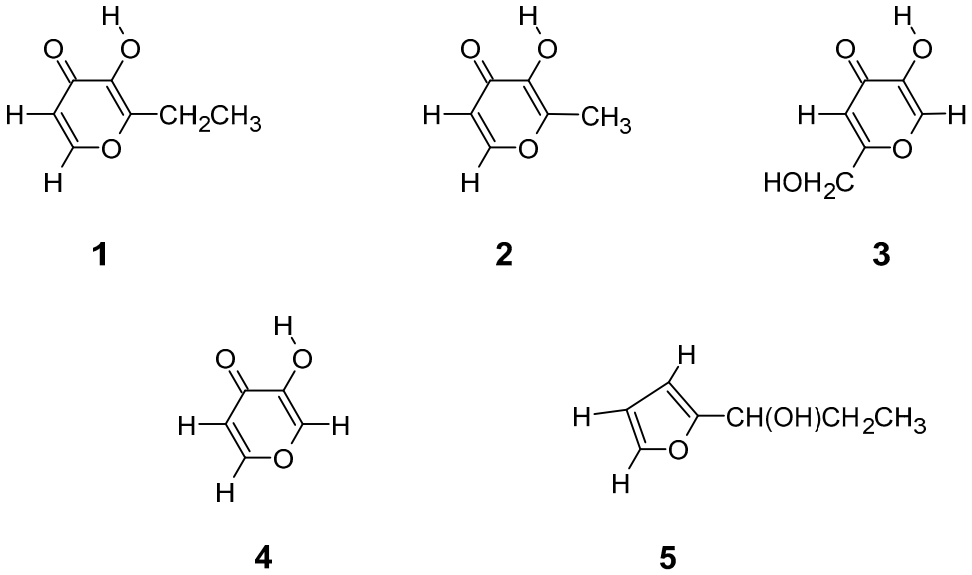
Copyright: © 2024 by the authors. Licensee MDPI, Basel, Switzerland. This article is an open access article distributed under the terms and conditions of the Creative Commons Attribution (CC BY) license (https://creativecommons.org/licenses/by/4.0/).

1. Introduction

Ethyl maltol (IUPAC name: 2-ethyl-3-hydroxy-4*H*-pyran-4-one; **1** in Scheme 1) is a widely utilized commercial flavor enhancer and stabilizer, commonly found in foods, beverages, medicines, tobacco products, perfumes, and cosmetics [1]. It appears as a white or nearly white crystalline powder with a sweet aroma reminiscent of caramelized sugar or cooked fruit. Unlike its precursor maltol (**2**), ethyl maltol is not naturally occurring and is produced synthetically. Over the past century, various methods have been developed for the synthesis of the compound from precursors such as kojic acid (**3**) [2], pyromeconic acid (**4**) [3], and especially ethylfurfuryl alcohol (**5**) [4], through processes including electrolysis, acidification, glycosidation, oxidation, or acidolysis [5–7]. For purification, binary aqueous ethanol mixtures are most commonly employed in recrystallization [6,7].

The maximum allowable daily intake of ethyl maltol for humans is 2 mg per kg of body weight [8]. In the tobacco industry, ethyl maltol is used as a flavoring agent, imparting a sweet or caramel taste to tobacco products, and it is commonly added to vaping liquids in many commercial e-cigarettes [9]. While many flavoring agents are used in low concentrations, ethyl maltol is typically utilized at concentrations exceeding

2 mg ml^{-1} [10], since it is regarded as nontoxic and highly pleasant to the human olfactory sense [11–13]. However, the use of ethyl maltol has raised recent concern, since it has been associated with enhanced copper-mediated cytotoxicity in lung epithelial cells [2], potentially increasing the risk of developing chronic lung disease [14].



Scheme 1. Ethyl maltol (**1**), maltol (**2**), kojic acid (**3**), pyromeconic acid (**4**), and ethylfurfuryl alcohol (**5**).

Maltol and its derivatives, including ethyl maltol, are significant ligands due to their pharmaceutical relevance, particularly in their role as d-metal transporters to cells, such as in the treatment of anemia [15] and diabetes [16–20]. These compounds can function as bidentate or bridging ligands [21–23], making them valuable for forming structurally complex polymeric metal-organic complexes [24,25]. Maltol and ethyl maltol readily form complexes with various metals, including magnesium [26], vanadium [27–29], and nickel [30].

Crystalline ethyl maltol exists in three distinct polymorphic forms, where the molecules are organized in nearly planar or tridimensional spiral chains, or form hydrogen-bonded dimeric structures [31]. In each polymorph, the hydroxyl group participates in intermolecular O–H···O hydrogen bonding with the carbonyl oxygen atom of a neighboring molecule [31]. However, in isolated molecules of ethyl maltol, the hydroxyl group is likely to form an intramolecular hydrogen bond with the carbonyl group, given their vicinal positioning within the molecule (see Scheme 1).

In this article, we present a comprehensive study combining theoretical analysis and infrared spectroscopy (covering both mid- and near-infrared (IR) regions) of ethyl maltol isolated in a low-temperature argon matrix at 14.5 K. The conformational landscape of ethyl maltol, together with its centrosymmetric dimer and possible photoproducts, was explored using density functional theory (DFT), providing a foundation for interpreting the experimental results, including the UV-induced photochemistry ($\lambda > 235$ nm) observed for the matrix-isolated compound and matrix annealing.

2. Experimental Methods

Ethyl maltol, sourced from Sigma-Aldrich (Saint Louis, MO, USA, purity > 99%), was used as received. Matrix isolation experiments were conducted using argon (Air Liquide, Istanbul, Türkiye, N60) as the matrix medium, with low-temperature conditions maintained by an APD Cryogenics closed-cycle helium refrigerator equipped with a DE-202A expander. A small quantity of the solid compound was placed in a custom-built variable temperature Knudsen cell, which was connected to the cryostat's vacuum chamber

via a needle valve kept at room temperature (~298 K) throughout the experiments. The compound was sublimated at approximately 358–368 K and co-deposited with a large excess of argon onto a CsI optical substrate cooled to 14.5 K. The substrate temperature was controlled and monitored at the sample holder using a silicon diode sensor connected to a digital controller (Scientific Instruments, Istanbul, Türkiye, model 9650–1), ensuring temperature stability within 0.1 K.

IR spectra were recorded using a Thermo Nicolet 6700 FTIR spectrometer, equipped with a deuterated triglycine sulphate (DTGS) detector and a Ge/KBr beam splitter for mid-IR measurements (4000−400 cm^{-1}; 0.5 cm^{-1} spectral resolution) or a CaF_2 beam splitter for near-IR measurements (7500−4000 cm^{-1}; 1.0 cm^{-1} spectral resolution). To prevent interference from atmospheric H_2O and CO_2, the spectrometer was continuously purged with a stream of dry, CO_2-filtered air.

Broadband UV light ($\lambda > 235$ nm) irradiation was carried out using a 500 W Hg(Xe) arc lamp (Newport, Oriel Instruments, Stratford, CT, USA) with the output power set to 200 W, directed through the outer quartz window of the cryostat and filtered through water.

3. Computational Details

Quantum chemical calculations were carried out using Gaussian 09 (revision A.02) [32], applying the DFT(B3LYP)/6–311++G(d,p) [33–38] level of theory. All geometries were optimized under TIGHT or VERY TIGHT convergence criteria, and the nature of each stationary point was verified by analyzing the corresponding Hessian matrix. All optimized structures were confirmed to be true minimum-energy conformations on the relevant potential energy surfaces. Harmonic IR spectra were generated at the same level of theory and simulated using Lorentzian functions with a full-width-at-half-maximum (FWHM) of 5 cm^{-1}. To account for basis set limitations, the approximate theoretical method, and anharmonicity, the calculated wavenumbers were scaled by factors of 0.940 above 3200 cm^{-1}, 0.960 for the 3200–2200 cm^{-1} region, and 0.980 below 2200 cm^{-1}. The vibrational analysis was performed with help of the vibrations' animation module of Chemcraft (version 1.8) [39] or Gaussview 5.0.9 [40].

4. Results and Discussion

4.1. DFT Calculations: Conformers, Relative Energies, and Isomerization Barriers

Ethyl maltol has two conformationally relevant internal degrees of freedom, which correspond to the internal rotations around C–O(H) and C–C(H_2CH_3) bonds. A search on the potential energy surface of the compounds undertaken at the B3LYP/6–311++G(d,p) level of theory yielded two different conformers (Figure 1I,II), both having a symmetry-equivalent form. The calculated relative electronic energies, zero-point corrected relative energies, standard Gibbs energies (298 K), and estimated room-temperature gas-phase equilibrium populations of the conformers are given in Table 1. Cartesian coordinates of the optimized geometries are provided in Table S1 (Supporting Information).

Table 1. B3LYP/6–311++G(d,p) calculated relative electronic energies (ΔE_{el}), zero-point corrected energies (ΔE_0), standard Gibbs energies (ΔG^0), and estimated gas-phase RT equilibrium populations (*Pop.*) of the conformers of ethyl maltol [a].

	I	II
ΔE_{el}	0.0	44.6
ΔE_0	0.0	42.7
ΔG^0	0.0	41.9
Pop. (%)	100.0	2×10^{-6}

[a] Energies in kJ mol^{-1} (see Figure 1 for structures of the conformers).

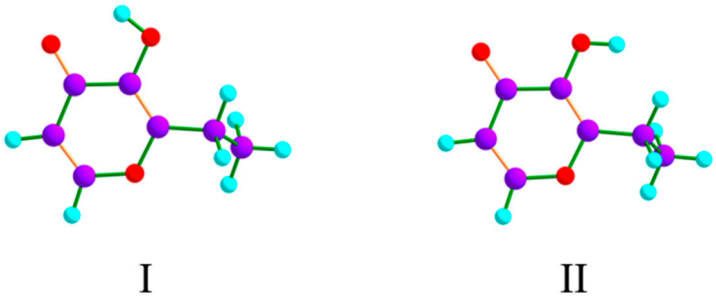


Figure 1. DFT(B3LYP)/6–311++G(d,p) calculated conformers of ethyl maltol.

The lowest energy conformer of ethyl maltol (conformer I) is stabilized by an O–H···O intramolecular hydrogen bond ($d_{O\cdots O}$ = 2.655 Å, $d_{O\cdots H}$ = 2.053 Å, ∠O–H···O = 117.9°). In this conformer, the O–C–C–CH_3 dihedral is ±69.6°, and its entropy at room temperature (RT) is 393.9 J mol^{-1} K^{-1}. Conformer II has the OH group rotated by 180° relative to its position in the most stable conformer I and is higher in energy by 44.6 kJ mol^{-1} (zero-point uncorrected value; 42.7 kJ mol^{-1} upon consideration of this correction). In conformer II, both the O–C–C–CH_3 dihedral angle (± 77.7°) and RT entropy (399.3 J mol^{-1} K^{-1}) are slightly larger than in the most stable conformer. Breaking the intramolecular hydrogen bond and rotating the hydroxy group when going from conformer I to II leads to a decrease in the C=O and O–H bond lengths of 0.013 Å (1.236 Å in I vs. 1.223 Å in II) and 0.014 Å (0.977 Å vs. 0.963 Å), respectively, i.e., both these bonds become stronger, while the O···O bond distance increases by 0.059 Å (2.655 Å vs. 2.714 Å) due to the steric repulsion between the lone electron pairs of the oxygen atoms.

The slightly larger O–C–C–CH_3 dihedral angle in conformer II (by 8.1°), compared to conformer I, can be rationalized considering the repulsion between the hydroxyl hydrogen atom and the nearest methylene hydrogen atom in this conformer (see Figure 1), which forces the latter atom to move out of the ring plane in the direction that also increases the distance between the ring and methyl group. This is reflected in the larger value calculated for the distance between the hydroxy oxygen atom and the hydrogen atom of the CH_2 group (2.693 Å in II, vs. 2.542 Å in I), the distance between the interacting hydrogen atoms in II being 1.978 Å. In conformer I, a bond-dipole/bond-dipole interaction is present, which is established between the nearly anti-parallelly aligned C–O(H) and C–H (CH_2) bonds, favoring the placement of the two bonds almost in the same plane (the two bonds are deviated by 11° from planarity in conformer I vs. 21° in conformer II).

The higher entropy of conformer II, compared to conformer I, reveals the larger conformational mobility in the first conformer and can be assigned to the fact that in this form the O–H···O intramolecular hydrogen bond is absent.

The potential energy profiles for the ground-state interconversion between the ethyl maltol conformers were calculated by performing relaxed potential energy scans using steps of 5° along the relevant isomerization coordinates (Figure S1, in Supporting Information). The highest energy conformer II can be easily transformed into the most stable conformer I through rotation of the OH group by crossing a small barrier of ~2.8 kJ mol^{-1} (zero-point corrected value; 44.5 kJ mol^{-1} in the reverse direction). Interconversions between the symmetry-equivalent forms, by rotation of the ethyl group around the C–C(H_2CH_3) bond, have associated barriers of 10.5 and 12.0 kJ mol^{-1} for I → I′ and II → II′, respectively.

4.2. IR Spectrum of Matrix-Isolated Ethyl Maltol

Molecules of ethyl maltol were isolated in an Ar matrix at 14.5 K, as described in Section 2. The IR spectrum of the prepared matrix is presented in Figure 2, where it can be compared with the B3LYP/6–311++G(d,p) calculated IR spectrum of conformer I. The calculated IR spectrum of conformer II is provided in Figure S2 (Supporting Information).

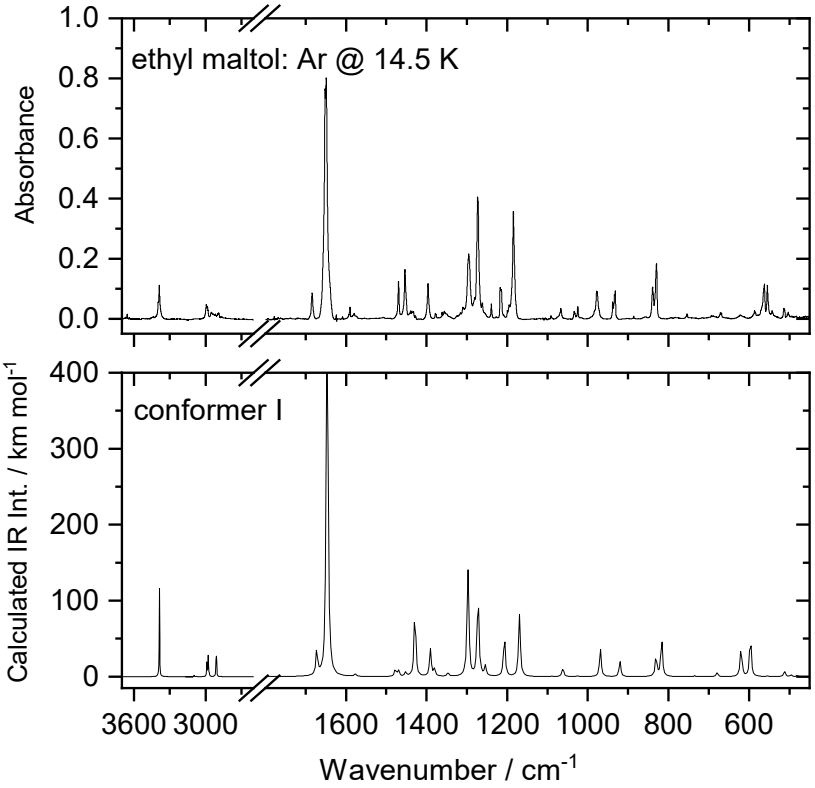


Figure 2. As-deposited IR spectrum of ethyl maltol isolated in an Ar matrix, at 14.5 K (top) and B3LYP/6–311++G(d,p) calculated (scaled) IR spectrum of conformer I of the molecule (bottom).

As shown in Figure 2, the predicted spectrum of conformer I of ethyl maltol agrees very well with the experimentally obtained spectrum. The hypothetical presence in the matrix of conformer II can be safely ruled out, since its IR spectrum is predicted to be considerably different from that of conformer I and unable to describe properly the experimental spectrum. For example, the band ascribable to the OH stretching vibration of ethyl maltol is observed at 3397/3387 cm^{-1} (site split band), at the expected frequency for conformer I (calculated value: 3387 cm^{-1}), while the OH stretching mode for conformer II is predicted to occur at a much higher frequency (3606 cm^{-1}). Besides, the experimental band shows a rather broad profile, which is consistent with the involvement of the OH group in the intramolecular H-bond characteristic of conformer I. The good consistency of the observed vs. calculated OH stretching band for conformer I and absence of any significant band for higher frequency values in the experimental spectrum are clear indications of the sole presence of conformer I in the as-deposited matrix. This result is also in consonance with the calculated relative energies of the two conformers reported above.

Analysis of the fingerprint spectral region further reinforces the conclusion that conformer I is the only form present in the as-deposited matrix: (i) calculations predict that for conformer I, in the 1700–1550 cm^{-1} spectral range, a low-intensity band (35.4 km mol^{-1}) ascribed mostly to the C=C stretching of the ring bond made by the carbons bearing the OH and ethyl substituents (with a smaller contribution from the hydroxyl in-plane bending deformation), ν(C=C) + δ(OH), should be observed at a higher frequency than the intense band (532.4 km mol^{-1}) due to the carbonyl stretching mode (1672 vs. 1646 cm^{-1}, respectively); this profile fits the experimental data, while for conformer II the order of the two bands is predicted to be the reverse (ν(C=O): 1683 cm^{-1}, intensity: 506.3 km mol^{-1}; ν(C=C) + δ(OH): 1639 cm^{-1}, intensity: 60.5 km mol^{-1}); (ii) contrary to what happens for conformer I, the predicted spectral profile for conformer II in the 1500–1100 cm^{-1} spectral range strongly differs from the experimental profile (compare Figures 2 and S2); (iii) the intense band (86.7 km mol^{-1}) predicted for conformer II at 1160 cm^{-1} ($\nu(CO)_{ring}$) does not have an experimental counterpart; (iv) the relatively intense bands observed experimentally

between 570 and 550 cm^{-1}, which correspond well to the calculated bands for conformer I at 620 and 597 cm^{-1}, have no correspondence in the predicted spectrum of conformer II.

The assignment of the experimental spectrum was facilitated by its good reproducibility by the calculations and is given in Table 2. Here, we will just briefly comment on some of the structurally most relevant assignments.

Table 2. Assignment of the IR spectrum of the as-deposited ethyl maltol isolated in an Ar matrix (conformer I) [a].

N	ν_{Exp}	ν_{Calc}	I_{Calc}	Assignment [b]
48	3397, 3387	3387	117.7	ν(OH)
47	n.obs.	3095	2.0	νs(CH)
46	n.obs.	3078	0.4	νas(CH)
45	2999/2995	2989	19.4	νas″(CH_3) + νas(CH_2)
44	2986/2980	2978	30.6	νas′(CH_3)
43	2957/2953/2949	2969	2.9	νas(CH_2) + νas″(CH_3)
42	2917/2913	2913	30.0	νs(CH_3)
41	2899/2890	2909	16.2	νs(CH_2)
40	1684	1672	35.4	ν(C=C) + δ(OH)
39	1652/1649	1646	532.4	ν(C=O)
38	1580	1577	3.4	ν(CH=CH)
37	1470	1478	9.0	δ′(CH_3)
36		1470	8.5	δ″(CH_3)
35	1454	1452	5.8	δ(CH_2)
34	1440/1437/1433	1429	88.3	ν(C=O–COH) + δ(OH)
33	1396	1391	36.4	δs(CH) + ν(CC) + δ(OH)
32	1378	1380	10.1	δs(CH_3)
31	1355	1347	5.6	wagg(CH_2)
30	1295	1298	154.1	δ(OH)
29	1273/1272	1272	117.3	twist(CH_2)
28	1239	1254	13.2	δa(CH) + ν(C–OH)
27	1217/1215	1207	57.7	ν(C=O–CH) + ν(C–OH)
26	1185	1170	84.5	ν(CO)ring + ν(C–OH)
25	1092	1089	0.4	γ″(CH_3)
24	1067	1062	12.1	γ′(CH_3)
23	1025	1026	1.0	ν(C–CH_2) + ν(CH_2–CH_3)
22	983/977/972	969	36.0	ν(CO)ring
21	938/932	932	0.1	γa(CH)
20		920	19.9	ν(CH_2–CH_3)
19	839/837	831	28.8	δ(CH–CH–O)ring
18	831/830	817	49.9	γs(CH)
17	777 (?)	769	0.2	γ(CH_2) + γ″(CH_3)
16	754	735	1.1	γ(C=O)
15	693/689/680	679	5.2	Ring breathing
14	570/564/562	620	40.6	γ(CC) + τ(OH)
13	555/551	597	53.6	τ(OH)
12	542	555	1.0	δ(C=O)
11	513/511	512	7.6	τ Ring
10	504/503	496	2.4	δ Ring
9	486/483	480	1.3	δ Ring
8	n.i.	340	6.6	δ Ring
7	n.i.	318	10.9	τ Ring + δ(CCC)ethyl
6	n.i.	287	6.4	δ(C–ethyl)
5	n.i.	251	0.8	τ Ring
4	n.i.	199	0.4	τ(CH_3)
3	n.i.	161	3.2	τ Ring
2	n.i.	98	0.0	δ(CCC)ethyl
1	n.i.	44	0.3	τ(C–CH_2)

[a] Frequencies in cm^{-1}; calculated intensities (I_{Calc}) in km mol^{-1}; calculated frequencies scaled by 0.940 above 3200 cm^{-1}, 0.960 in the region of 3200–2200 cm^{-1}, and 0.980 below 2200 cm^{-1}, respectively. [b] ν, stretching; δ, in-plane bending; γ, out-of-plane rocking; τ, torsion; n.obs., not observed; n.i., not investigated; (?), uncertain.

The assignment of the CH stretching modes should be considered as tentative, because of the predicted close proximity in frequency of the different modes, their usually low intensity in the matrix medium, and complexity due to overtones and combination tones that also appear in this spectral region and, in some cases, participate in Fermi resonance interactions. As mentioned above, the OH appears as a site split doublet at 3397/3387 cm^{-1}, while the C=O stretching mode gives rise to the pair of bands observed at 1652/1649 cm^{-1}, split by Fermi resonance interaction with the first overtone of the CH ring out-of-plane rocking mode, γ_s(CH). The in-plane-bending CH vibrations of the aromatic ring are observed at 1396 cm^{-1} (symmetric mode) and 1239 cm^{-1} (anti-symmetric), in good agreement with the theoretical predictions (1391 and 1254 cm^{-1}, respectively). The ring C=C stretching modes are observed at 1684 and 1580 cm^{-1} (calculated values: 1672 and 1577 cm^{-1}, respectively).

The ring C–O stretching modes are ascribed to the bands observed at 1185 cm^{-1} (mostly C_{ethyl}–O) and 983/977/972 cm^{-1} (essentially C_H–O) and are predicted at 1170 and 969 cm^{-1}, respectively. According to the calculations, the hydroxyl C–O_H stretching coordinate contributes to several modes giving rise to bands in the 1450–1390 cm^{-1} range (see Table 2). The calculations indicate that the COH in-plane bending also contributes significantly to several vibrations (Table 2), but its major contribution is to the band predicted at 1298 cm^{-1}, which is ascribed to the intense band observed experimentally at 1295 cm^{-1} as a broad band, as expected due to the involvement of the OH group in the intramolecular H-bond. In turn, the out-of-plane mode (OH torsion, τ(OH)) is ascribed to the band at 555/551 cm^{-1}, slightly downshifted in frequency relative to the calculated value (597 cm^{-1}). Another predicted intense band is observed at 1273/1272 cm^{-1}, which according to the calculations corresponds to the twisting of the CH_2 group, and is predicted at 1272 cm^{-1}.

In the NIR region, the band ascribable to the 1st overtone of the νOH vibration (2ν(OH)) is observed at 6955 cm^{-1}, shifted by ca. 170 cm^{-1} in relation to the expected harmonic frequency for this vibration (~6785 cm^{-1}, as calculated from the average value of the two observed bands assigned to the νOH fundamental vibration), demonstrating the considerable anharmonicity of the OH stretching coordinate in the studied molecule.

4.3. Annealing Experiments

The deposited argon matrix of ethyl maltol was subjected to annealing by increasing the temperature of the matrix from the deposition temperature (14.5 K) to 41.5 K, in steps of 2 K. The changes due to the annealing were followed by IR spectroscopy. Until 28.5 K, no significant spectral changes were observed. Above this temperature, noticeable spectral changes occur, which could be assigned to aggregation of the compound, the main new features in the spectrum of the annealed matrix being very well reproduced by the spectrum of the centrosymmetric dimer of ethyl maltol (Figures 3 and S3).

The total intensity ratio of the theoretically calculated spectra of the dimer and the monomer in the studied region is 4.70. In the experimental spectrum, this ratio is found to be 2.56, as measured from the total areas under the bands, indicating that the ratio of dimer to monomer in the matrix after the annealing is about 1:2, i.e., about 50% of the monomer underwent aggregation. Note, however, that in Figure 3, the intensity of the calculated spectrum of the dimer was divided by 4 (instead of 2), to obtain a better visual comparison between the calculated and experimental spectra when peak maxima intensities are considered, because the bands of the dimer are systematically broader than those of the monomer.

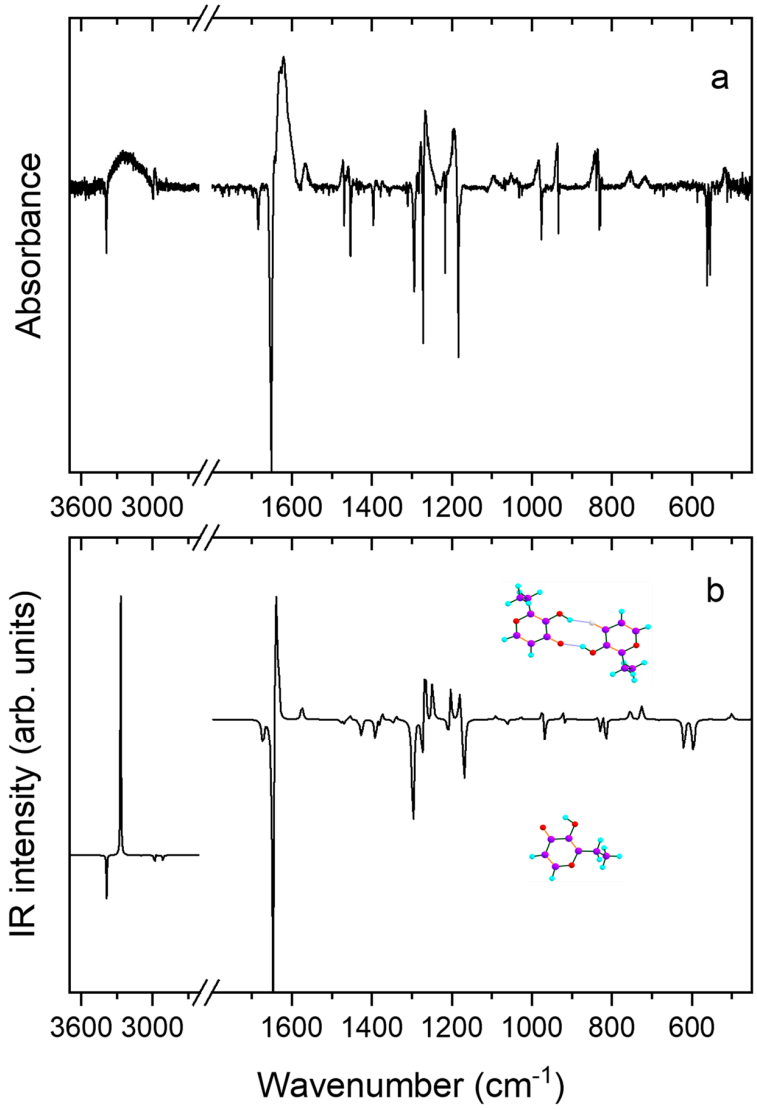


Figure 3. Difference IR spectrum of ethyl maltol in an Ar matrix (41.5 K *minus* as-deposited matrix) (**a**), and B3LYP/6–311++G(d,p) simulated IR difference spectrum (centrosymmetric dimer *minus* conformer I) (**b**). In the calculated (scaled) spectrum, IR intensities of the dimer were divided by 4; the intensity scale before and after the break are different to allow a better comparison with the experiment.

The monomer of ethyl maltol (C_1 symmetry) has 48 active vibrations, all being active in infrared. On the other hand, the centrosymmetric dimer is C_i symmetry, and its vibrations span the irreducible representations $51A_g + 51\ A_u$, with the A_u modes being active in infrared while the A_g are Raman active. Among the active modes, 48 are intramolecular modes, whereas the remaining 3 correspond to intermolecular vibrations. The intermolecular modes are, however, of low frequency, below the experimentally studied spectral region, so that the bands observed in the measured spectrum of the dimer and the monomer have essentially a one-to-one correspondence. Table 3 presents the assignments for the IR active bands of ethyl maltol dimer in the studied spectral region. The complete vibrational data, including Raman active modes, are given in Table S2.

Table 3. Assignment of the IR spectrum of the centrosymmetric dimer of ethyl maltol (composed of two molecular units in the conformation of form I) in an Ar matrix [a].

N	ν_{Exp}	ν_{Calc}	I_{Calc}	Assignment [b]
51	3248	3268	3332.2	ν(OH)
50	n.obs.	3030	6.5	νs(CH)
49	n.obs.	3077	0.7	νas(CH)
48	2980	2990	31.1	νas″(CH_3) + νas(CH_2)
47		2976	63.0	νas′(CH_3)
46		2969	20.6	νas(CH_2) + νas″(CH_3)
45	2922 (?)	2912	46.2	νs(CH_2)
44	2883	2910	68.2	νs(CH_3)
43	1644/1641	1642	1354.3	ν(C=O) + ν(C=C)
42	1625	1634	347.3	ν(C=O) + ν(C=C) + δ(OH)
41	1565/1548	1575	85.4	ν(CH=CH)
40	1475	1477	21.8	δ′(CH_3)
39		1469	13.7	δ″(CH_3)
38	1459	1454	42.0	δ(CH_2)
37	1435	1429	245.4	ν(C=O–COH) + ν(C–OH)
36	1390	1388	49.6	δs(CH)
35	1374	1376	47.6	δs(CH_3)
34	1353	1340	20.5	wagg(CH_2)
33	1285	1291	16.1	twist(CH_2)
32	1278	1269	536.5	ν(CO)ring + δ(OH)
31	1266	1249	218.7	δ(OH)
30	1196	1204	261.1	ν(C=O–CH) + ν(C=O–COH)
29		1180	166.9	ν(CO)ring + ν(C–OH)
28	1092	1091	18.2	γ″(CH_3) + γ(CH_2)
27	1053/1048	1062	21.1	γ′(CH_3)
26	1039	1028	14.0	ν(CO)ring + γ′(CH_3)
25	983	972	110.5	ν(C–CH_2) + ν(CH_2–CH_3)
24	937	926	5.0	γa(CH)
23		921	100.7	ν(CH_2–CH_3)
22	842	834	73.3	δ(CH–CH–O)ring
21	835	819	119.2	γs(CH)
20	n.obs.	769	1.1	γ(CH_2) + γ″(CH_3)
19	752	755	49.1	τ(OH)
18	716	726	79.6	γ(C=O) + τ(OH)
17	689	678	18.4	Ring breathing
16	n.obs.	613	1.1	γ(CC)
15	561	554	5.5	δ(C=O)
14	516	512	29.9	τ Ring
13	508	502	23.4	δ Ring
12		497	17.2	δ Ring

[a] Frequencies in cm^{-1}; calculated intensities (I_{Calc}) in km mol^{-1}; calculated frequencies scaled by 0.940 above 3300 cm^{-1}, 0.960 in the region of 3300–2200 cm^{-1}, and 0.980 below 2200 cm^{-1}, respectively. [b] ν, stretching; δ, in-plane bending; γ, out-of-plane rocking; τ, torsion; n.obs., not observed; (?), uncertain.

Since in the dimer the O–H···O hydrogen bond interactions (intermolecular) are stronger than in the monomer (intramolecular), as seen by the calculated shorter $d_{O\cdots H}$ distance in the dimer (1.783 Å vs. 2.053 Å in the monomer), longer r_{O-H} bond (0.983 Å vs. 0.977 Å), and larger ∠O–H···O angle (153.3° vs. 117.9°), the OH stretching band in the dimer appears significantly shifted to lower frequencies (Δν(OH) = –139 cm^{-1}; calculated: –119 cm^{-1}) and shows the characteristic very high intensity and broad profile for a strong hydrogen bond system, while the OH torsional mode appears considerably blue shifted compared to its position in the monomer (Δν ~ 200 cm^{-1}; calculated: 158 cm^{-1}) and is also observed as a broad feature, in agreement with the expectations [41–46]. On the other hand, the fact that the δ(OH) bending coordinate contributes significantly to several modes both in the monomer and in the dimer (see Tables 2 and 3) precludes any attempt to define a characteristic frequency shift when going from the monomer to the dimer.

The energies of the intramolecular O–H···O bond in conformer I and of the intermolecular H bonds in the dimer can be estimated using the vibrational data, together with application of the empirical correlations between the vibrational frequency shifts upon H-bond formation and the H-bond energies derived for the first time by Jogansen [41].

According to Jogansen [41], the H-bond energy (ΔH, in kJ mol^{-1}) and the downshift in the ν(OH) stretching vibration of an H-bond donor upon H-bond formation ($\Delta\nu_{OH}$ = ν(OH)^o–ν(OH), where ν(OH)^o is the frequency of the free OH group; cm^{-1}) obey the correlation:

$$(\Delta H)^2 = 1.92\ [\Delta\nu(OH) - 40] \quad (1)$$

While an alternative correlation also exists [41–46] between the H-bond energy and the upshift in the τ(OH) torsional vibration:

$$\Delta H = 0.67\ (\Delta\tau(OH))^2 \quad (2)$$

where $(\Delta\tau_{OH})^2 = 10^{-4}\ \{\tau(OH)^2 - [\tau(OH)^o]^2\}$, τ(OH)^o being the torsional frequency in the free OH group.

To apply correlations (1) and (2), the frequencies calculated (and scaled as described in Section 3) for conformer II, where the OH group is free, can be used as reference values for ν(OH)^o (3606 cm^{-1}) and τ(OH)^o (290 cm^{-1}). The calculated H-bond energies obtained from correlation (1) for the intramolecular bond in conformer I and for the dimer are 19 and 25 kJ mol^{-1}, respectively, while those obtained from correlation (2) are 15 and 32 kJ mol^{-1}, yielding average values for the hydrogen bonds of 17 and 28 kJ mol^{-1}, respectively.

It is worth mentioning that the DFT calculated difference in energy between the centrosymmetric dimer and two units of conformer I is –35.8 kJ mol^{-1}. This energy can be defined as the total stabilization energy upon dimerization (or binding energy). If it were assumed that this stabilization was only due to H-bonding, the energy of each H-bond in the dimer would be 17.9 kJ mol^{-1}. This value is indeed lower than those resulting from the empirical correlations based on the experimental data, as it could be anticipated, since it does not take into account other structural changes upon dimer formation and, in particular, the energy increase due to the break of the intramolecular H-bond (i.e., the sum of the energies of the two H-bonds in the dimer must be higher than the binding energy to compensate for the energy increase due to the break of the two intramolecular hydrogen bonds pre-existing in the monomeric units).

4.4. UV-Induced Photochemistry of Matrix-Isolated Ethyl Maltol

The matrix-isolated ethyl maltol was irradiated with broadband UV light (λ > 235 nm) provided by a 500 W Hg(Xe) arc lamp, as described in the experimental section. The experimental ultraviolet absorption spectra of ethyl maltol in 1,4-dioxane, chloroform and methanol and the calculated gas-phase TD-DFT(B3LYP)/6–311++G(d,p) spectrum exhibit the absorption maximum at 274, 277, 276, and 269 nm, respectively (Figure S4), which, according to the calculations, should be assigned to the $S_1 \leftarrow S_0$ transition (Table S3). Hence, the irradiation was performed in the shorter wavelength wing of the band associated with this transition, that corresponds to the LUMO←HOMO ($\pi^* \leftarrow \pi$) transition (Figure S5).

The irradiation led to a decrease in intensity of the bands of ethyl maltol initially present in the IR spectrum and simultaneous emergence of new bands. The spectroscopic data are shown in Figures 4 and 5. Figure 6 summarizes the observed processes.

Immediately after the start of the irradiation, noticeable changes were observed in the spectra. Two distinct sets of new bands were identified: one that reached a maximum after ca. 1 min of irradiation, when the amount of reactant was reduced to ~2/3 of the initial, and then started to decrease, and a second that persisted in the spectra until all reactant was consumed, after 20 min of irradiation.

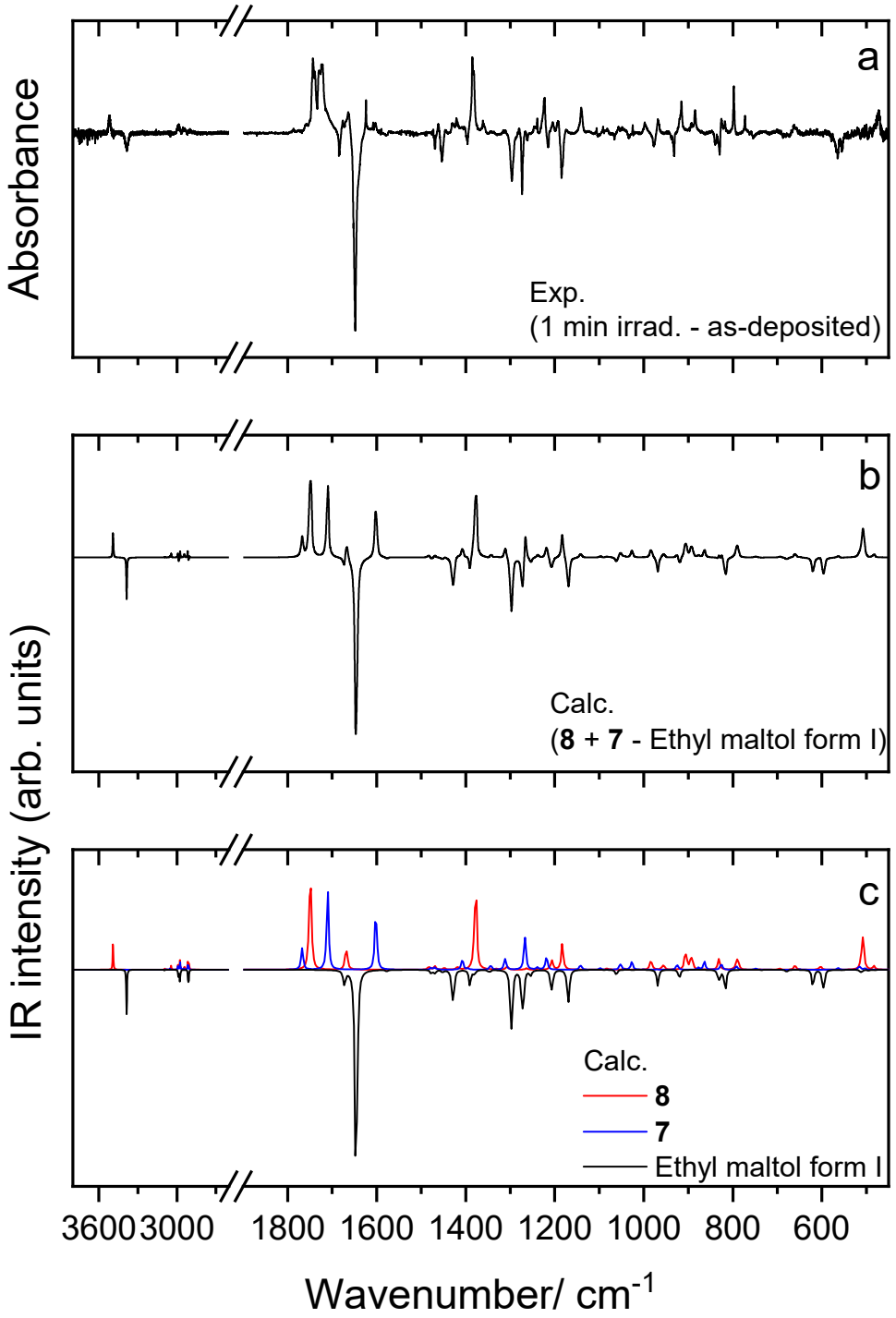


Figure 4. Difference IR spectrum obtained by subtracting the spectrum of the as-deposited Ar matrix of ethyl maltol from that obtained after 1 min of irradiation ($\lambda > 235$ nm) (**a**), and simulated spectra constructed based on the DFT(B3LYP)/6–311++G(d,p) calculated IR spectra of the identified photoproducts (**7** and **8**; see Figure 6) and of ethyl maltol (conformer I) (**b**,**c**). In the calculated spectra, the frequencies were scaled as described in Section 3, and the intensities were multiplied by different factors for each compound to facilitate comparison with the experimental data.

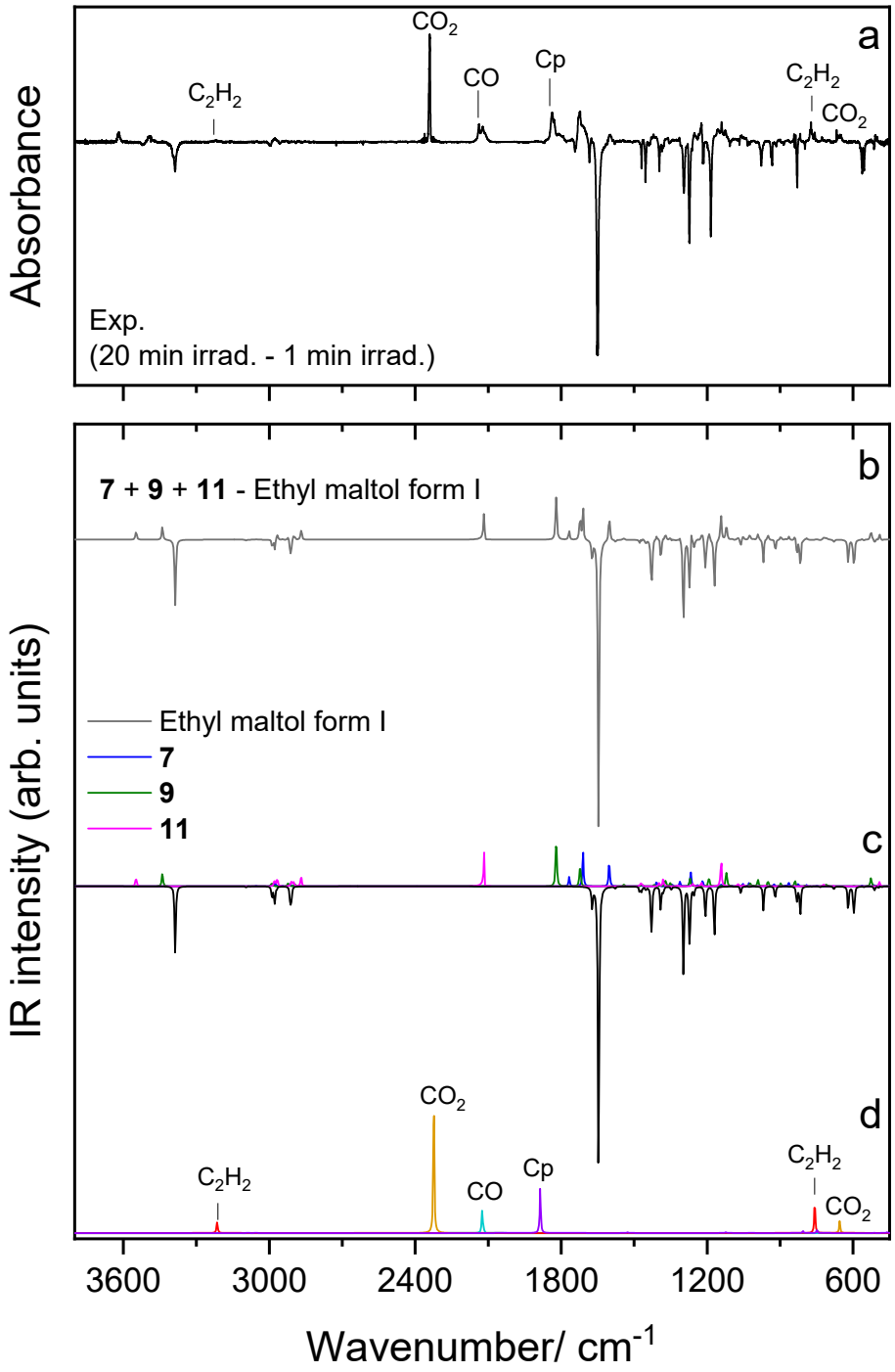


Figure 5. Difference IR spectrum obtained by subtracting the spectrum of 1 min irradiated Ar matrix of ethyl maltol from that obtained after 20 min of irradiation ($\lambda > 235$ nm) (**a**), and simulated spectra constructed based on the DFT(B3LYP)/6–311++G(d,p) calculated IR spectra of the identified photoproducts **7**, **9,** and **11** (see Figure 6) and of ethyl maltol (conformer I) (**b**,**c**), and of smaller molecules resulting from photolysis (**d**). The spectra of these latter species are shown separate from those of **7**, **9**, **11,** and ethyl maltol for better viewing, and the spectrum of compound **8** (that are pointing down in the experimental spectrum) were omitted from spectra b and c for simplicity since they correspond to comparatively small features. Cp denotes cyclopropenone. In the calculated spectra, frequencies were scaled as described in Section 3, and intensities were multiplied by different factors for each compound to facilitate comparison with the experimental data.

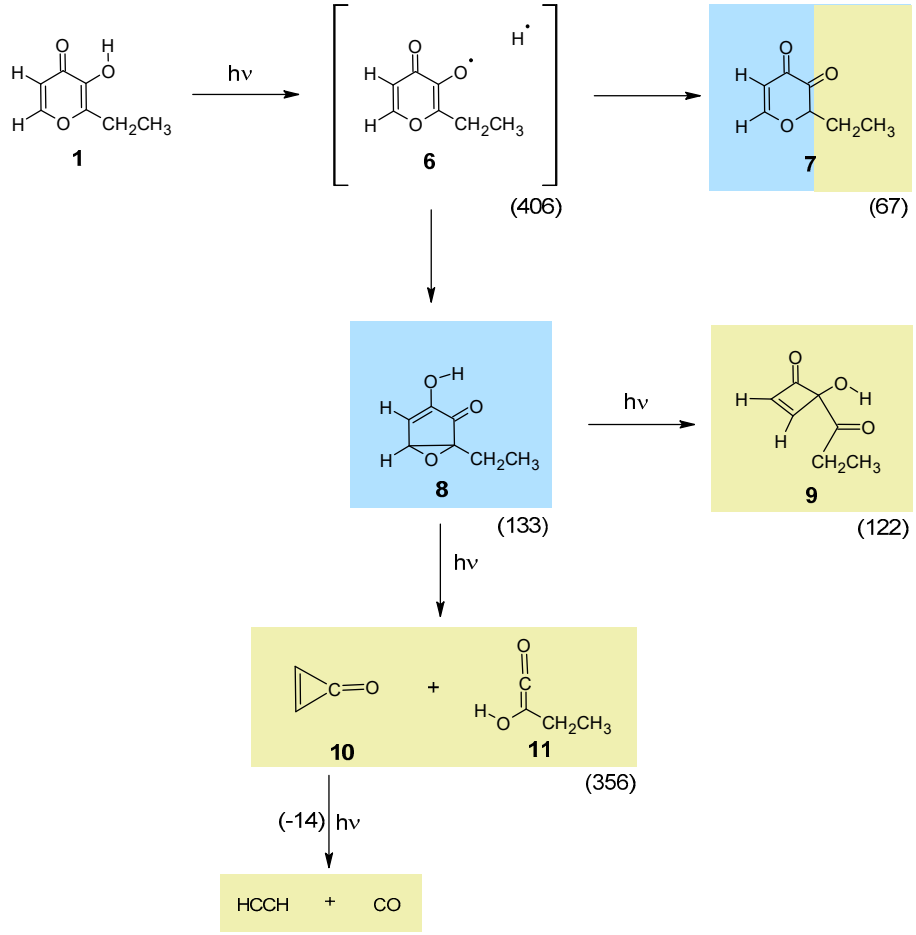


Figure 6. Proposed reaction scheme for the results of irradiation of ethyl maltol in an argon matrix (λ > 235 nm). The radical **6** was not observed. Products **7** and **8** were observed after 1 min of irradiation (blue squares). The latter was subsequently transformed into other species. The products observed after 20 min of irradiation are represented in green squares. The numbers in parentheses correspond to the electronic energies of the different species relative to the reactant, in the ground electronic state, except in the case of the number associated with the cyclopropenone photodecomposition that corresponds to the decrease in electronic energy of the reaction.

Figure 4 presents the difference experimental IR spectra built by subtracting the spectrum of the as-deposited matrix from the spectrum of the sample after 1 min of irradiation. This spectrum is compared in the figure with the simulated difference IR spectrum constructed based on the DFT(B3LYP)/6–311++G(d,p) calculated spectra of the photogenerated species (bands pointing up) and of the reactant species (ethyl maltol form I; bands pointing down).

The structural complexity of ethyl maltol made the identification of the photoproducts a tough task, and calculations were undertaken in a large series of potential photoproducts. The best matches for the two photoproducts observed after 1 min of irradiation were 1-ethyl-3-hydroxy-6-oxibicyclo [3.1.0] hex-3-en-2-one (**8** in Figure 6) and 2-ethyl-2*H*-pyran-3,4-dione (**7**), the first corresponding to the product that undergoes subsequent reactions upon continued irradiation, and the second being the persistent species. These two photoproducts can be obtained from ethyl maltol via the (non-observed) radical **6**, resulting from the homolytic photocleavage of the hydroxyl bond, after recombination with the hydrogen atom in the matrix cage. Photocleavage of phenolic-type OH groups for matrix-isolated compounds has been observed previously, including for the parent phenol compound [47–49], the reaction shown to take place via the photoinduced detachment-attachment (PIDA) mechanism first described in detail by Sobolewski and coworkers [50],

who have highlighted the role in this mechanism of the excited πσ* states, which have a repulsive character along the O–H stretching coordinate [50,51]. The initially formed phenoxy radical has been detected for some matrix-isolated phenols [47–49], but has proved to be elusive in other cases, because of rapid recombination [52–54]. For ethyl maltol, the recombination is very fast and the radical **6** could not be observed. The two initially observed photoproducts are the species resulting from recombination at the two closest positions relative to that of the hydroxyl group undergoing photocleavage, in agreement with the expectations. The calculations show that the radical has an energy ca. 406 kJ mol^{-1} above ethyl maltol, in the ground state, while the observed photoproducts **7** and **8** resulting from the recombination of the phenoxy radical **6** with the hydrogen atom have energies 67 and 133 kJ mol^{-1} above ethyl maltol, and 339 and 273 kJ mol^{-1} below **6**, respectively, *i.e.*, **7** is considerably more stable than **8**.

Mark bands of **8** are observed at 3517 (ν(OH)), 1742/1728 (ν(C=O)), 1664 (ν(C=C)), 1384/1360 and 1140 ($\nu(C_{OH}–C_{=O})$ + δ(COH), 2 modes), 997 ($\nu(CH_2–CH_3)$), 966 (δ_{as}(CH–CH) + $\nu(C_H–C_H)$), 915 ($\gamma'(CH_3)$), 884 ($\nu_s(CO)_{epoxy}$), 798 (γ(C=O)), and 473 (τ(OH)) cm^{-1}, corresponding to calculated values of 3491, 1749, 1668, 1378, 1183, 984, 956, 906, 893, 790, and 508 cm^{-1}, respectively; those of **7** are observed at 1790/1759 (ν(C=O)), 1724/1714 (ν(C=O)), 1604 (ν(C=C)), 1420 (δ(CH–CH) + $\nu(C_H–C_{=O})$), 1224 ($\nu_{as}(CO)_{ring}$), and 1025 (ν(C–CH_2) + $\nu(CH_2–CH_3)$) cm^{-1}, and predicted at 1768, 1710, 1602, 1408, 1267, and 1027 cm^{-1}, respectively. The full calculated IR spectra for these compounds and the assignment of the major bands are provided in the Supporting Information (Table S4), while their optimized Cartesian coordinates are given in Table S5.

Figure 5 shows the difference experimental IR spectra built by subtracting the spectrum after 1 min of irradiation from that obtained after 20 min of irradiation, when the reactant has been exhausted. The figure presents also the simulated difference IR spectrum built based on the DFT(B3LYP)/6–311++G(d,p) calculated spectra of the photogenerated species (bands pointing up) and of the reactant species (ethyl maltol form I, bands pointing down; photoproduct **8** is also consumed and its bands are also observed in the experimental difference spectrum pointing down as expected; however, these bands have been omitted in the simulated difference spectrum shown in the figure in the quest of simplicity since they correspond to comparatively small features). In the figure, the spectra of all fragmentation products except **11** are presented separately from those of rearrangement products (**7**, **9**) for better viewing.

Several products were found to be present in the photolyzed matrix at the end of the irradiation (20 min). Besides **7**, which was already present in noticeable amount after 1 min of irradiation as described above, the rearrangement product 4-hydroxy-4-propanoylcyclobut-2-en-1-one (**9** in Figure 6) and several fragmentation products were identified.

Product **9** is most probably a result of photorearrangement of **8**, as indicated in Figure 6. Its most characteristic bands were observed at 3491 (ν(OH)), 1836/1829 ($\nu(C=O)_{ring}$, the first band also assigned to cyclopropenone), 1724 (ν(C=O)), 1251 (δ_{as}(CH–CH) + δ(COH)), 1125 (δ(COH) + $\gamma'(CH_3)$ + $\nu(C_{OH}–C_{=O})$), 705 ($\gamma(C=O)_{ring}$), and 507 (τ(OH)) cm^{-1}. These bands are predicted by the calculations to occur at 3439, 1820, 1722, 1270, 1121, 709, and 527 cm^{-1}, respectively, in very good agreement with the experimental data.

The fragmentation products include cyclopropenone (**10**) and 2-hydroxybut-1-en-1-one (**11**), which can be formed together from **8**, acetylene (C_2H_2) and carbon monoxide (CO), which are the products of fragmentation of cyclopropenone, and carbon dioxide (CO_2) that is most probably produced in secondary processes that we were unable to identify. Carbon monoxide and CO_2 are promptly recognized by their characteristic bands at 2138 cm^{-1} (CO) [55,56], and 2340 ($\nu_{as}(CO_2)$) and 662/650 ($\delta(CO_2)$) cm^{-1} [57,58]. Acetylene bands were observed at 3222 (ν_{as}(CH)) and 772 (δ_{as}(CH) cm^{-1}. For the isolated molecule, these bands were observed in argon matrix at 3303/3289 and 737 cm^{-1} [59], respectively, indicating that the acetylene molecules in the ethyl maltol photolyzed matrix are interacting with other species in the matrix cage in a way that significantly affects the position of the bands. In agreement with this conclusion is also the broad profile observed for the ν_{as}(CH) stretching

mode, which is more sensitive to intermolecular effects than the bending vibration [59]. Cyclopropenone bands were observed at 1836 (ν(C=O)), 798 (δ(C=O)) and 757 (γ(C=O)) cm^{-1}, the first being also assigned to **9**. These bands were previously reported at 1840, 853 and 788 cm^{-1} for the net compound [60], while the DFT(B3LYP)/6–311++G(d,p) calculated frequencies for the isolated molecule are 1886, 805 and 748 cm^{-1}, respectively. Mark bands for **11** were observed at 3612 (ν(OH)), 2123 (ν_{as}(C=C=O)), 1152 (ν(CO) + δ(COH)), and 500 (γ(C=C=O)) cm^{-1}, which are in correspondence with the calculated values 3548, 2155, 1143 and 492 cm^{-1}, respectively.

Table S6 provides the full calculated IR spectra for compounds **9**, **10** and **11** and the assignment of the major observed bands. The optimized Cartesian coordinates for these compounds are given in Table S7.

5. Conclusions

Ethyl maltol was investigated by matrix (Ar; 14.5 K) isolation infrared spectroscopy. DFT(B3LYP)/6–311++G(d,p) calculations were used to help interpret the experimentally obtained data.

In the as-deposited matrix, the compound was found to exist in a sole conformer (form I), characterized by possessing an intramolecular O–H···O hydrogen bond, whose energy was estimated as ~17 kJ mol^{-1}. The IR spectrum of this conformer (in the 4000–450 cm^{-1} region) was described and assigned. The molecular structure of this conformer and that of the higher-energy conformer II (bearing a free OH group) were studied in detail theoretically on a comparative basis, and the potential energy landscape of the compound was investigated to understand the reasons for the conformers' relative stability and their isomerization dynamics.

Annealing of the matrix up to 41.5 K allowed observation of aggregation of the ethyl maltol, predominantly to the centrosymmetric dimer where the molecules assume the conformation of the most stable conformer for the isolated molecule (conformer I). The IR spectrum of the dimer was assigned and the energy of the H-bonds present in the dimer was estimated to be 28 kJ mol^{-1} (per bond) using the obtained vibrational data and Jogansen's [41] empirical correlations between the vibrational frequency shifts of the ν(OH) and τ(OH) modes upon H-bond formation and the H-bond energies.

The UV-induced photochemistry (λ > 235 nm) of the matrix-isolated ethyl maltol was also investigated. Excitation was carried out at the shorter wavelength wing of the band associated with the $S_1 \leftarrow S_0$ transition, which corresponds to the LUMO ← HOMO ($\pi^* \leftarrow \pi$) transition. Immediately after the irradiation began, noticeable changes appeared in the spectra. Two distinct sets of new bands were identified: the first set reached its maximum intensity after approximately one minute of irradiation, at which point the reactant had decreased to about two-thirds of its initial amount, and then began to diminish. The second set of bands persisted in the spectra until the reactant was completely consumed, which occurred after 20 min of irradiation. These two photoproducts were identified as 1-ethyl-3-hydroxy-6-oxibicyclo [3.1.0] hex-3-en-2-one (**8** in Figure 6) and 2-ethyl-2*H*-pyran-3,4-dione (**7**), resulting from rearrangements of the initially formed ethyl maltol radical (**6**) through the PIDA mechanism [50–54] after recombination with the hydrogen atom in the matrix cage. These photoproducts are the species resulting from recombination at the two closest positions relative to that of the hydroxyl group undergoing photocleavage, in agreement with the expectations.

Photoproduct **8** was subsequently converted into different products, which include 4-hydroxy-4-propanoylcyclobut-2-en-1-one (**9**), by rearrangement, and cyclopropenone (**10**) and 2-hydroxybut-1-en-1-one (**11**), as a result of photofragmentation. Other final products were also observed, specifically acetylene and CO (the expected fragmentation products of cyclopropenone), and CO_2.

The IR spectra of all the observed photoproducts were calculated and assignments for the corresponding observed experimental bands were given.

A relevant conclusion of this study for practical applications of the compound is that it was shown to promptly react upon excitation in the UV ($\lambda > 235$ nm). In Ar matrix, 1/3 of the compound was shown to be photochemically converted in about 1 min of irradiation, and its complete consumption occurred in ca. 20 min only.

Supplementary Materials: The following supporting information can be downloaded at: https://www.mdpi.com/article/10.3390/spectroscj2040013/s1, Figure S1 showing the potential energy profiles for the conformational isomerizations in ethyl maltol; Figure S2 with a comparison of the as-deposited spectrum of ethyl maltol in Ar matrix with the calculated spectrum of conformer II; Figure S3 showing the experimental and TD-DFT calculated UV spectra of ethyl maltol; Figure S4 showing the representation of the calculated relevant orbitals for ethyl maltol (conformer I). Tables S1, S5, and S7 with the optimized Cartesian coordinates of the two conformers of ethyl maltol and of the observed photoproducts; Table S2, with the calculated vibrational frequencies, IR intensities, and Raman activities for the centrosymmetric dimer of ethyl maltol; Table S3, presenting the TD-DFT calculated excitation energies and oscillator strengths for the 3 lowest singlet states of ethyl maltol (conformer I); Tables S4 and S6, with the calculated vibrational frequencies and IR intensities and assignments for the observed photoproducts (**7**, **8**, **9**, **10**, **11**).

Author Contributions: İ.S., laboratory work, computations, funding acquisition, data analysis, writing (original draft); S.L., methodology, laboratory work, data analysis; T.N., methodology, laboratory work; Y.G.S., laboratory work, funding acquisition; R.F., conceptualization, formal analysis, supervision, funding acquisition, writing (final version). All authors have read and agreed to the published version of the manuscript.

Funding: The authors greatly appreciate Bitlis Eren University Research Foundation for providing computing resources and the Portuguese Science Foundation ("*Fundação para a Ciência e a Tecnologia*"—FCT) for funding CQC-IMS through projects UIDB/00313/2020 (DOI: 10.54499/UIDB/00313/2020), UIDP/00313/2020 (DOI: 10.54499/UIDP/00313/2020), and LA/P/0056/2020—National Funds. FCT is also acknowledged for financial support to the project PTDC/QUI-QFI/1880/2020 (QUANTUN).

Institutional Review Board Statement: Not applicable.

Informed Consent Statement: Not applicable.

Data Availability Statement: Not applicable.

Acknowledgments: Coimbra Laser Lab (CLL) is acknowledged for experimental facilities.

Conflicts of Interest: The authors declare no conflicts of interest.

References

1. Pittet, A.O.; Rittersbacher, P.; Muralidhara, R. Flavor properties of compounds related to maltol and isomaltol. *J. Agric. Food Chem.* **1970**, *18*, 929–933. [CrossRef]
2. Ichimoto, I.; Ueda, H.; Tatsumi, C.; Fujii, K.; Sekido, F.; Nonomura, S. Studies on kojic acid and its related γ-pyrone compounds: Part VII. The alkylation of kojic acid and pyromeconic acid through their Mannich base (synthesis of maltol-(1)) Part VIII. Synthesis of comenic acid from kojic acid (synthesis of maltol (2)). *Agric. Biol. Chem.* **1965**, *29*, 94–103.
3. Popoff, T.; Theander, O.; Westerlund, E. Formation of aromatic compounds from carbohydrates. VI. Reaction of dihydroxyacetone in slightly acidic, aqueous solution. *Acta Chem. Scand. B* **1978**, *32*, 1–7. [CrossRef]
4. Shono, T.; Matsumura, Y. Novel syntheses of maltol and related compounds. *Tetrahed. Lett.* **1976**, *17*, 1363–1364. [CrossRef]
5. Sun, J.J.; Hao, M.; Wang, L.; Cui, L.H. Research on the synthesis process of ethylmaltol by electrochemistry. *Appl. Mech. Mater.* **2013**, *284*, 380–384. [CrossRef]
6. Fung, F.-N.; Hay, B.A.; Swenarton, J.E. Method of Synthesizing Gamma Pyrones. 1999. Available online: https://patents.google.com/patent/US5908941A/en (accessed on 17 May 2024).
7. Weeks, P.D.; Allingham, R.P. Preparation of Gamma-Pyrone İntermediates. 1984. Available online: https://patents.google.com/patent/US4451661A/en (accessed on 17 May 2024).
8. Gralla, E.J.; Stebbins, R.B.; Coleman, G.L.; Delahunt, C.S. Toxicity studies with ethyl maltol. *Toxic. Appl. Pharm.* **1969**, *15*, 604–613. [CrossRef]
9. Durrani, K.; El Din, S.-M.A.; Sun, Y.; Rule, A.M.; Bressler, J. Ethyl maltol enhances copper mediated cytotoxicity in lung epithelial cells. *Toxic. Appl. Pharm.* **2021**, *410*, 115354. [CrossRef]

10. Omaiye, E.E.; Luo, W.; McWhirter, K.J.; Pankow, J.F.; Talbot, P. Ethyl maltol, vanillin, corylone and other conventional confectionery-related flavour chemicals dominate in some e-cigarette liquids labelled 'tobacco' flavoured. *Tobacco Contr.* **2022**, *31*, s238–s244. [CrossRef]
11. Burdock, G.A. *Fenaroli's Handbook of Flavor İngredients*, 5th ed.; CRC Press: Boca Raton, FL, USA, 2005.
12. Rennhard, H.H. Metabolism of ethyl maltol and maltol in the dog. *J. Agric. Food Chem.* **1971**, *19*, 152–154. [CrossRef]
13. LeBlanc, D.T.; Akers, H.A. Maltol and ethyl maltol: From the larch tree to successful food additive. *Food Technol.* **1989**, *43*, 78–84.
14. McAlinden, K.D.; Lu, W.; Eapen, M.S.; Sohal, S.S. Electronic cigarettes: Modern instruments for toxic lung delivery and posing risk for the development of chronic disease. *Int. J. Biochem. Cell Biol.* **2021**, *137*, 106039. [CrossRef] [PubMed]
15. Thompson, K.H.; Barta, C.A.; Orvig, C. Metal complexes of maltol and close analogues in medicinal inorganic chemistry. *Chem. Soc. Rev.* **2006**, *35*, 545–556. [CrossRef]
16. Thompson, K.H.; Lichter, J.; LeBel, C.; Scaife, M.C.; McNeill, J.H.; Orvig, C. Vanadium treatment of type 2 diabetes: A view to the future. *J. Inorg. Biochem.* **2009**, *103*, 554–558. [CrossRef]
17. Thompson, K.H.; Orvig, C. Vanadium in diabetes: 100 years from Phase 0 to Phase I. *J. Inorg. Biochem.* **2006**, *100*, 1925–1935. [CrossRef]
18. Kawabe, K.; Yoshikawa, Y.; Adachi, Y.; Sakurai, H. Possible mode of action for insulinomimetic activity of vanadyl (IV) compounds in adipocytes. *Life Sci.* **2006**, *78*, 2860–2866. [CrossRef] [PubMed]
19. Peters, K.G.; Davis, M.G.; Howard, B.W.; Pokross, M.; Rastogi, V.; Diven, C.; Greis, K.D.; Eby-Wilkens, E.; Maier, M.; Evdokimov, A. Mechanism of insulin sensitization by BMOV (bis maltolato oxo vanadium); unliganded vanadium (VO_4) as the active component. *J. Inorg. Biochem.* **2003**, *96*, 321–330. [CrossRef]
20. Willsky, G.R.; Goldfine, A.B.; Kostyniak, P.J.; McNeill, J.H.; Yang, L.Q.; Khan, H.R.; Crans, D.C. Effect of vanadium (IV) compounds in the treatment of diabetes: In vivo and in vitro studies with vanadyl sulfate and bis (maltolato) oxovandium (IV). *J. Inorg. Biochem.* **2001**, *85*, 33–42. [CrossRef] [PubMed]
21. Kennedy, D.C.; Patrick, B.O.; James, B.R. Cationic ruthenium(III) maltolato–imidazole complexes—Synthesis; characterization; antiproliferatory activity, Adapted from the Ph.D. thesis of D.C. Kennedy. *Can. J. Chem.* **2011**, *89*, 948–958. [CrossRef]
22. Chin, L.F.; Kong, S.M.; Seng, H.L.; Khoo, K.S.; Vikneswaran, R.; Teoh, S.G.; Ahmad, M.; Khoo, S.B.A.; Maah, M.J.; Ng, C.H. Synthesis, characterization and biological properties of cobalt (II) complexes of 1,10-phenanthroline and maltol. *J. Inorg. Biochem.* **2011**, *105*, 339–347. [CrossRef]
23. Hsieh, W.-Y.; Zaleski, C.M.; Pecoraro, V.L.; Fanwick, P.E.; Liu, S. Mn (II) complexes of monoanionic bidentate chelators: X-ray crystal structures of $Mn(dha)_2(CH_3OH)_2$ (Hdha= dehydroacetic acid) and $[Mn(ema)_2(H_2O)]_2 \cdot 2H_2O$ (Hema= 2-ethyl-3-hydroxy-4-pyrone). *Inorg. Chim. Acta* **2006**, *359*, 228–236. [CrossRef]
24. Szklarzewicz, J.; Paciorek, P.; Zabierowski, P.; Kurpiewska, K.; Mikuriya, M.; Yoshioka, D. Synthesis, crystal structures and spectroscopy studies of Mo (IV) complexes synthesized in reactions with kojic acid, maltol and ethylmaltol. *Polyhedron* **2012**, *37*, 35–41. [CrossRef]
25. Chen, X.-F.; Wang, T.-R.; Ma, Z.; Yu, Y.; Tang, L.; Jin, L.-Y.; Sheng, G.-H.; Zhu, H.-L. Synthesis, crystal structures and insulin-like activity of two new oxidovanadium (V) complexes with aroylhydrazones and maltol mixed-ligands. *Polyhedron* **2017**, *137*, 321–324. [CrossRef]
26. Case, D.R.; Gonzalez, R.; Zubieta, J.; Doyle, R.P. Synthesis, characterization, and cellular uptake of magnesium maltol and ethylmaltol complexes. *ACS Omega* **2021**, *6*, 29713–29723. [CrossRef] [PubMed]
27. Xue, L.-W.; Han, Y.-J.; Luo, X.-Q. Synthesis, crystal structures and antimicrobial activity of oxidovanadium (V) complexes with hydrazone and pyrone ligands. *Acta Chim. Sloven.* **2019**, *66*, 622–628. [CrossRef]
28. Xue, L.-W.; Han, Y.-J.; Luo, X.-Q. Six-coordinated oxidovanadium (V) complexes derived from hydrazone and pyrone ligands: Synthesis, spectroscopy, and catalytic property. *Inorg. Nano-Met. Chem.* **2020**, *50*, 654–660. [CrossRef]
29. Bergeron, A.; Kostenkova, K.; Selman, M.; Murakami, H.A.; Owens, E.; Haribabu, N.; Arulanandam, R.; Diallo, J.-S.; Crans, D.C. Enhancement of oncolytic virotherapy by vanadium (V) dipicolinates. *Biometals* **2019**, *32*, 545–561. [CrossRef]
30. Alblawi, K.; Henderson, W.; Nicholson, B.K. Synthesis and characterization of nickel (II) maltolate complexes containing ancillary bisphosphine ligands. *J. Coord. Chem.* **2011**, *64*, 679–687. [CrossRef]
31. Brown, S.D.; Burgess, J.; Fawcett, J.; Parsons, S.A.; Russell, D.R.; Waltham, E. Three polymorphic forms of 2-ethyl-3-hydroxy-4-pyranone (ethyl maltol). *Acta Cryst. Sect. C Cryst. Struct. Com.* **1995**, *51*, 1335–1338. [CrossRef]
32. Frisch, M.J.; Trucks, G.W.; Schlegel, H.B.; Scuseria, G.E.; Robb, M.A.; Cheeseman, J.R.; Scalmani, G.; Barone, V.; Mennucci, B.; Petersson, G.A.; et al. *Gaussian 09 (Revision A.02)*; Gaussian, Inc.: Wallingford, CT, USA, 2016.
33. Becke, A.D. Density-functional exchange-energy approximation with correct asymptotic behavior. *Phys. Rev. A* **1988**, *38*, 3098–3100. [CrossRef]
34. Lee, C.; Yang, W.; Parr, R.G. Development of the Colle-Salvetti correlation-energy formula into a functional of the electron density. *Phys. Rev. B* **1988**, *37*, 785–789. [CrossRef]
35. Vosko, S.H.; Wilk, L.; Nusair, M. Accurate spin-dependent electron liquid correlation energies for local spin density calculations: A critical analysis. *Can. J. Phys.* **1980**, *58*, 1200–1211. [CrossRef]
36. McLean, A.D.; Chandler, G.S. Contracted Gaussian basis sets for molecular calculations. I. Second row atoms, Z= 11–18. *J. Chem. Phys.* **1980**, *72*, 5639–5648. [CrossRef]

37. Clark, T.; Chandrasekhar, J.; Spitznagel, G.W.; Schleyer, P.V.R. Efficient diffuse function-augmented basis sets for anion calculations. III. The 3-21+G basis set for first-row elements, Li–F. *J. Comput. Chem.* **1983**, *4*, 294–301. [CrossRef]
38. Frisch, M.J.; Pople, J.A.; Binkley, J.S. Self-consistent molecular orbital methods 25. Supplementary functions for Gaussian basis sets. *J. Chem. Phys.* **1984**, *80*, 3265–3269. [CrossRef]
39. Andrienko, G.A. *Chemcraft (Version 1.8), Graphical Software for Visualization of Quantum Chemistry Computations*; Chemcraft Holdings, Inc.: Port Hope, ON, Canada, 2024.
40. Frisch, A.; Hratchian, H.P.; Dennington, R.D., II; Keith, T.A.; Millam, J.; Nielsen, B.; Holder, A.J.; Hiscocks, J. *GaussView Version 5.0.8*; Gaussian, Inc.: Wallingford, CT, USA, 2009.
41. Iogansen, A.V. Direct proportionality of the hydrogen bonding energy and the intensification of the stretching ν(XH) vibration in infrared spectra. *Spectrochim. Acta A* **1999**, *55*, 1585–1612. [CrossRef]
42. Reva, I.D.; Fausto, R.; Rozenberg, M.; Shoham, G. Low temperature FTIR spectra and hydrogen bonding in polycrystalline L-alanine. *Spectrochim. Acta A* **2003**, *59*, 3253–3266.
43. Rozenberg, M.; Shoham, G.; Reva, I.D.; Fausto, R. Low temperature FTIR spectra and hydrogen bonding in cytosine polycrystals. *Spectrochim. Acta A* **2004**, *60*, 463–470. [CrossRef]
44. Rozenberg, M.; Shoham, G.; Reva, I.D.; Fausto, R. Low temperature Fourier transform infrared spectra and hydrogen bonding in polycrystalline uracil and thymine. *Spectrochim. Acta A* **2004**, *60*, 2323–2336. [CrossRef]
45. Rozenberg, M.; Shoham, G.; Reva, I.D.; Fausto, R. Spontaneous self-association of adenine and uracil in polycrystals from low temperature FTIR spectra in the range below 1000 cm^{-1}. *Spectrochim. Acta. A* **2005**, *62*, 233–238. [CrossRef]
46. Rozenberg, M.; Shoham, G.; Reva, I.D.; Fausto, R. A correlation between the proton stretching vibration red shift and the hydrogen bond length in polycrystalline amino acids and peptides. *Phys. Chem. Chem. Phys.* **2005**, *7*, 2376–2383. [CrossRef]
47. Giuliano, B.M.; Reva, I.; Lapinski, L.; Fausto, R. Infrared spectra and ultraviolet-tunable laser induced photochemistry of matrix-isolated phenol and phenol-d_5. *J. Chem. Phys.* **2012**, *136*, 024505. [CrossRef] [PubMed]
48. Nowak, M.J.; Reva, I.; Jesus, A.J.L.; Lapinski, L.; Fausto, R. UV-promoted radical formation, and near-IR-induced and spontaneous conformational isomerization in monomeric 9-methylguanine isolated in low-temperature Ar matrices. *Phys. Chem. Chem. Phys.* **2019**, *21*, 22857–22868. [CrossRef] [PubMed]
49. Jesus, A.J.L.; Júnior, J.R.L.; Fausto, R.; Reva, I. Infrared spectra and phototransformations of *meta*-fluorophenol isolated in argon and nitrogen matrices. *Molecules* **2022**, *27*, 8248. [CrossRef] [PubMed]
50. Sobolewski, A.L.; Domcke, W.; Dedonder-Ladeux, C.; Jouvet, C. Excited-state hydrogen detachment and hydrogen transfer driven by repulsive $^1\pi\sigma^*$ states: A new paradigm for nonradiative decay in aromatic biomolecules. *Phys. Chem. Chem. Phys.* **2002**, *4*, 1093–1100. [CrossRef]
51. Vieuxmaire, O.P.; Lan, Z.; Sobolewski, A.L.; Domcke, W. Ab initio characterization of the conical intersections involved in the photochemistry of phenol. *J. Chem. Phys.* **2008**, *129*, 224307. [CrossRef]
52. Kuş, N.; Reva, I.; Bayarı, S.; Fausto, R. In situ photoproduction of dichlorodibenzo-*p*-dioxin from non-ionic triclosan. *J. Mol. Struct.* **2012**, *1007*, 88–94. [CrossRef]
53. Jesus, A.J.L.; Fausto, R.; Reva, I. Conformational space; IR-induced, and UV-induced chemistry of carvacrol isolated in a low-temperature argon matrix. *J. Phys. Chem. A* **2021**, *125*, 8215–8229. [CrossRef]
54. Jesus, A.J.L.; Nunes, C.M.; Reva, I. Conformational structure, infrared spectra and light-induced transformations of thymol isolated in noble gas cryomatrices. *Photochem* **2022**, *2*, 405–422. [CrossRef]
55. Abe, H.; Takeo, H.; Yamada, K.M. Infrared spectroscopy of CO trapped in an argon matrix revisited. *Chem. Phys. Lett.* **1999**, *311*, 153–158. [CrossRef]
56. Dubost, H. Infrared absorption spectra of carbon monoxide in rare gas matrices. *Chem. Phys.* **1976**, *12*, 139–151. [CrossRef]
57. Dahoo, P.R.; Berrodier, I.; Raducu, V.; Teffo, J.L.; Chabbi, H.; Lakhlifi, A.; Abouaf-Marguin, L. Splitting of vibrational n_2 mode of CO_2 isotopic species in the unstable trapping site in argon matrix. *Eur. Phys. J. D* **1999**, *5*, 71–81. [CrossRef]
58. Jacox, M.E.; Milligan, D.E. Vibrational spectrum of CO_2^- in an argon matrix. *Chem. Phys. Lett.* **1974**, *28*, 163–168. [CrossRef]
59. Jose, K.V.J.; Gadre, S.R.; Sundararajan, K.; Viswanathan, K.S. Effect of matrix on IR frequencies of acetylene and acetylene-methanol complex: Infrared matrix isolation and ab initio study. *J. Chem. Phys.* **2007**, *127*, 104501. [CrossRef] [PubMed]
60. Tuazon, E.C.; Finseth, D.H.; Miller, F.A. Cyclopropenone: Normal coordinate calculation and the form of the normal modes. *Spectrochim. Acta A* **1975**, *31*, 1133–1138. [CrossRef]

Disclaimer/Publisher's Note: The statements, opinions and data contained in all publications are solely those of the individual author(s) and contributor(s) and not of MDPI and/or the editor(s). MDPI and/or the editor(s) disclaim responsibility for any injury to people or property resulting from any ideas, methods, instructions or products referred to in the content.